Probing host-anaerobe interactions in innovative human gut cellular models

Blessing O. Anonye[a], Jack Hassall[b], Jamie Patient[c], Usanee Detamornrat[c], Afnan Aladdad[c], Stephanie Schüller[d,e], Felicity R.A.J Rose[c], Meera Unnikrishnan [a#]

[a]Microbiology and Infection Unit, Division of Biomedical Sciences, Warwick Medical School, University of Warwick, Coventry, United Kingdom

[b]Warwick Integrative Synthetic Biology Centre, School of Life Sciences, University of Warwick, Coventry, United Kingdom

[c]Division of Regenerative Medicine and Cellular Therapies, School of Pharmacy, Centre for Biomolecular Sciences, University of Nottingham, Nottingham, United Kingdom

[d]Norwich Medical School, University of East Anglia, Norwich, United Kingdom

[e]Gut Health and Food Safety Programme, Quadram Institute Bioscience, Norwich, United Kingdom

Running title: Host-anaerobe interactions in human gut cellular models

[#] Address for correspondence: Meera Unnikrishnan, m.unnikrishnan@warwick.ac.uk

Abstract word count: 244

Text word count: 5069

KEYWORDS**:** *C. difficile*, adherence, 3-D gut epithelium, colonization, anaerobic, vertical diffusion chamber

ABSTRACT

Interactions of anaerobic gut bacteria with the intestinal mucosa have been poorly studied due to challenges in culturing anaerobes with the oxygen-requiring gut epithelium. Gut colonization by the anaerobic pathogen *Clostridium difficile*, a leading cause of hospital-acquired diarrhea, is a key determinant of disease outcome. However, precise mechanisms of mucosal attachment and spread remain unclear. Here, using human gut cells co-cultured within controlled dual environment chambers, we describe the dynamics of *C. difficile* infection. We demonstrate that *C. difficile* adheres and multiplies as micro-communities when grown on a mucin-producing Caco-2/HT29-MTX gut epithelial cell layer. Prolonged infection causes redistribution of actin and loss of epithelial integrity, accompanied by production of *C. difficile* spores, and interestingly *C. difficile* filamentation, a potentially new mechanism of *C. difficile* persistence. Intriguingly, we find that even in the absence of major *C. difficile* toxins, the bacterium is able to disrupt epithelial barrier function. To examine *C. difficile*-commensal interactions, we co-cultured *C. difficile* with the anaerobic gut commensal *Bacteroides dorei. B. dorei* adheres to gut cells and inhibits *C. difficile* multiplication. Furthermore, we have developed novel multilayer and three-dimensional gut models containing gut myofibroblasts. *C. difficile* adheres more efficiently to epithelial cells in these models compared to the monolayer systems, inducing a stronger chemokine response, indicating a role for myofibroblasts in early host responses to *C. difficile*. Our study describes new human gut models which effectively recreate the *C. difficile* infection process, and enable host-anaerobe and pathogen-commensal interaction studies *in vitro*.

IMPORTANCE

Understanding the host responses to anaerobic gut pathogens or commensals, and gaining mechanistic insights into the three-way interaction between pathogens, commensals and the gut epithelium is fundamental to advancing our knowledge of gut microbiome function. Host-pathogen interaction studies of the human anaerobic pathogen, *C. difficile* and other gut-associated anaerobes is challenging due to the lack of appropriate *in vitro* systems. In this study, employing novel two and three-dimensional models, we have tracked *C. difficile* infection over longer time scales, examining the attachment and invasion of the gut epithelium and the effects of key virulence factors. Furthermore, we demonstrate interactions of other important gut commensals like *Bacteroides* with the epithelium and with *C. difficile*. This study provides new insight into the molecular and cellular events that occur at the gut epithelial interface during infection.

INTRODUCTION

Clostridium difficile, an anaerobic spore-forming bacterium is the main cause of infectious diarrhea in healthcare settings. A major risk factor for *C. difficile* infection (CDI) is antibiotic use, which results in the disruption of the intestinal microbiota, allowing *C. difficile* to colonize and proliferate (1, 2). An increase in severe disease and deaths from CDI has been observed in the US, estimated at 453,000 cases, with 29,000 deaths (3). Estimates of about 13,000 cases were recorded in the UK and incidence of CDI have been reported across Europe, Canada and Australia (4-6).

83

84 *C. difficile* produces two main toxins, toxin A and toxin B (TcdA and TcdB), and some
85 strains produce a binary toxin (CDT), all of which contribute to bacterial pathogenicity.
86 Toxins A and B are known to disrupt the intestinal epithelial barrier function through
87 activation of the MAPK pathway leading to a cytokine response (7, 8). The key role for
88 toxins during infection has been demonstrated in mouse models using toxin mutants (7,
89 9). However, *C. difficile* colonization of the intestinal mucosa is a key factor in CDI, and
90 several bacterial factors such as surface layer proteins (10, 11), adhesins (12-14), cell
91 wall proteins (15) and flagella are thought to play a role in this process (16, 17).
92 Moreover, *C. difficile* is also known to produce spores that are resistant to antibiotics
93 and disinfectants (18, 19). These spores may serve as reservoir for recurrence of
94 infection in the host.

95

96 Although animal models of CDI have been used to understand *C. difficile* pathogenesis,
97 molecular mechanisms of bacterial interactions with the human gut mucosa are best
98 studied using *in vitro* human colon derived cell cultures. *In vitro* models enable
99 molecular and cellular studies on both the host and the pathogen, easier testing of
100 multiple conditions and visualization of infection dynamics. Infection of human intestinal
101 epithelial cell (IEC) lines has been used to study *C. difficile* pathogenesis but these
102 models have been limited to short time periods as *C. difficile* requires an anaerobic
103 environment for optimal growth (20-22). A dual environment system such as a vertical
104 diffusion chamber (VDC), which permits growth of the bacteria and IECs in appropriate
105 gaseous environments was used previously by Schüller and Phillips to demonstrate

106 increased adherence of enterohaemorrhagic *Escherichia coli* (EHEC) to polarized IECs
107 in microaerobic conditions, with enhanced expression and translocation of EHEC type
108 III secreted effector proteins (23). Similarly, an increase in *Campylobacter jejuni*
109 invasion of IECs was observed under a microaerobic environment in the VDC (24).
110 Recently, a VDC was employed to culture *C. difficile* with T84 cells where an anaerobic
111 environment was shown to enhance *C. difficile*-induced cytokine production, although
112 this was only studied over a short time course (25).
113
114 Models that replicate the physiology and local tissue environment found *in vivo* are ideal
115 for investigating host-pathogen interactions in IECs. Three-dimensional (3-D) gut
116 cellular models are more suited for epithelial cell growth and differentiation through
117 secretion of proteins such as growth factors by the underlying cells, and supporting
118 scaffolds can be designed to meet the cell type-specific needs (26, 27). Scaffolds
119 generated from natural or synthetic polymers such as matrigel, collagen and
120 polyethylene terephthalate (PET) have been used to generate the matrix (27, 28). More
121 recently, electrospinning has been employed to fabricate fibers from polymers creating
122 a structure similar to the natural fibrous network of the extracellular matrix (ECM) (26,
123 27). Electrospinning was used to create nanofiber and microfiber scaffolds for optimal 3-
124 D *in vitro* culture of airway epithelial and fibroblast cells (26). Fibroblast cells play an
125 active role in producing ECM, and producing chemokines in response to bacterial
126 infection (29).
127

128 Three-dimensional gut models have been employed to understand key bacterial and
129 host pathways in a range of pathogens including *C. difficile* (30, 31), *Salmonella* (32),
130 *Cryptosporidium parvum* (33) and Coxsackievirus B (34). In human intestinal organoids
131 infected with *C. difficile,* bacteria were reported to be viable for up to 12h (31), while a 3-
132 D model using Caco-2 cells grown as cysts in a matrigel monitored the adhesion and
133 translocation of *C. difficile* for 1h (30). While both studies investigated the role of *C.*
134 *difficile* toxins in these models, neither was able to follow the infection for a longer
135 period of time due to the lack of an optimal environment for bacterial growth.
136
137 In this study, we have determined the infection dynamics of *C. difficile* over an extended
138 time frame using novel human gut epithelium models. We demonstrate that *C. difficile*
139 adheres and forms communities over 24h, while it produces spores, toxins and bacterial
140 filamentous forms, accompanied by chemokine production over 48h in a monolayer
141 VDC model. Furthermore, we demonstrate that this system can be used to study
142 interactions of obligate anaerobes such as the gut commensal, *Bacteroides dorei*, with
143 IECs. Interestingly, we demonstrate that *B. dorei* inhibits *C. difficile* replication on gut
144 epithelial cells. Notably, in a complex 3-D model that we developed which contains
145 myofibroblasts on electrospun nanofiber scaffolds, we observed increased bacterial
146 adhesion to IECs and an enhanced host cell response, compared to the monolayer
147 model.
148
149
150 **RESULTS**
151
152 **Development of a gut cellular model for *C. difficile***

153 A polarized cell layer comprising IECs (epithelial Caco-2 and mucus producing HT29-
154 MTX goblet cells) was cultured on the apical side of a Snapwell insert as shown in Fig.
155 1. Inserts with polarized cell layers were placed in the VDC and experiments were
156 performed by perfusing a mixture of 5% CO_2 and 95% air in the basolateral
157 compartment for epithelial cell growth and an anaerobic gas mixture (10% CO_2, 80% N_2
158 and 10% H_2) on the apical side for bacterial growth. The barrier integrity of IECs was
159 monitored by measuring the transepithelial electrical resistance (TEER). The TEER
160 values demonstrated an intact epithelium in the control IECs incubated within the VDC,
161 although a slight decline was observed over 24h (Fig. 2A). However, no significant
162 disruption to the IECs was seen after 24h or 48h by microscopy; actin staining showed
163 that the cytoskeleton of the control cells was intact at 24h and 48h (Fig. 2B).
164 Immunofluorescent staining of the Snapwell inserts for MUC2, a major mucus protein
165 produced by goblet cells, showed that a small amount of mucus was produced (Fig.
166 S1).
167
168 Furthermore, growth of *C. difficile* in the apical compartment of the VDC for 3h was
169 compared to growth in the anaerobic cabinet. No significant differences were observed
170 indicating that the VDC maintained anaerobic conditions in the apical chamber (Fig.
171 S2).
172
173 ***C. difficile* colonization leads to disruption of the intestinal epithelium**
174 To determine how *C. difficile* interacts with the human host in the short and long term,
175 Caco-2/HT29-MTX layers were infected with *C. difficile* R20291 at an MOI of 100:1 for

176 different periods of time in the anaerobic chamber of the VDC (Fig. 1). In order to study
177 bacteria that adhere to the IECs and their replication, for all experiments, at 3h p.i., the
178 apical supernatant containing the *C. difficile* was removed, the IECs washed in PBS,
179 fresh pre-reduced media added, followed by incubation for the required time. The
180 number of adherent *C. difficile* was determined by counting colony forming units (CFUs)
181 from the cell lysates, after washing off non-adherent bacteria. A significant increase in
182 the number of cell-associated *C. difficile* was observed from 3h to 24h p.i. (Fig. 2C).
183 This increase in cell-associated bacteria corresponded to a decrease in TEER
184 measurements indicating disruption of the intestinal epithelial barrier (Fig. 2A). Confocal
185 microscopy showed *C. difficile* present as small micro-communities on the IECs. At
186 early time points (3h and 6h p.i.), there was little disruption of the actin filaments but at
187 24h and 48h p.i., destruction of the cytoskeleton was evident (Fig. 2D). Interestingly, at
188 48h p.i., immunofluorescent staining showed the presence of filamenting *C. difficile* (Fig.
189 2D).
190
191 **Prolonged infection is associated with spore and toxin production, and host**
192 **responses**
193 In order to fully understand bacterial factors necessary for CDI persistence, we
194 performed an extended infection for up to 48h in the 2-D monolayer epithelial model.
195 Spores, a major bacterial mechanism of persistence, were detected in the cell-
196 associated fraction and in the apical supernatants at 24h and 48h p.i. (Fig. 3A).
197
198 Toxin A was monitored over time during infection and while not detectable at early time
199 points, increased production was seen at 24h and 48h p.i. as determined by ELISA (Fig.

200 3B). Analysis of the basolateral supernatant for the host chemokine IL-8, which has
201 been previously implicated in *C. difficile* infection (35), revealed that IL-8 levels were low
202 at 6h p.i. but increased at 24h and 48h p.i. in the monolayer epithelial model (Fig. 3C).
203

204 **Major *C. difficile* toxins are not solely responsible for disruption of the epithelial**
205 **barrier**

206 As the toxins are considered to be the major virulence factors in CDI, we sought to
207 determine their effects on the epithelial cells. To do this, we utilized a triple toxin mutant
208 (ΔABCDTa) strain, which is unable to produce toxins A, B and the binary toxin (subunit
209 CdtA) (36) to perform adhesion assays on the gut epithelium. The absence of all three
210 toxins did not affect the adhesion of *C. difficile* to the IECs (Fig. 4A). As *C. difficile* toxins
211 are known to cause disruption to the tight junctions of the epithelium, leading to a more
212 permeable epithelial barrier, we measured the TEER to determine the effects of the
213 triple toxin mutant on the IECs. At 6h p.i., there was less disruption compared to the wild
214 type (WT) but at 24h p.i., there was no significant difference between the WT and the
215 triple mutant (Fig. 4B). Immunofluorescent staining indicated less redistribution of the
216 actin cytoskeleton at 24h p.i. compared to the WT strain (Fig. 4C).
217

218 **Co-culturing *C. difficile* with *Bacteroides dorei* results in *C. difficile* inhibition**
219 **within an epithelial gut model.**

220
221 To determine if our VDC-based cellular system could be extended for use with other
222 anaerobic bacteria, we studied a strict commensal anaerobe, *B. dorei* within the
223 monolayer epithelial model using similar conditions as for *C. difficile*. Adherence to the

224 IECs was determined at 3h and 24h by CFU counts, as described for *C. difficile*. *B.*
225 *dorei* adhered to the epithelial cells and multiplied over 24h, as observed for *C. difficile*
226 (Fig. 5A, B). *B. dorei* and *C. difficile* were then grown as mixed cultures in the VDC.
227 Cell-associated bacteria were quantitated by plating on a medium used to selectively
228 isolate *C. difficile* colonies, which also allowed the growth of *B. dorei*. *Bacteroides*
229 colonies were distinguished by colony size, color and morphology (small colonies). A
230 significant decrease in the number of *C. difficile* was observed when co-cultured with *B.*
231 *dorei* in the presence of IECs at 24h p.i. but not at 3h p.i. (Fig. 5A, B, $p < 0.001$). We
232 also observed higher colony counts when *B. dorei* was grown in co-culture with *C.*
233 *difficile* at 3h and 24h, compared to mono-cultures of *B. dorei* (Fig. 5A, B).
234

235 **Increased cell-associated bacteria in multilayer and 3-D models containing**
236 **fibroblast cells**

237 As the monolayer 2-D models do not optimally represent the human gut epithelium, we
238 developed this system further by increasing its cell complexity. Typically, a
239 myofibroblast layer underlies the basement membrane in the human gut. To incorporate
240 myofibroblasts into our model, human CCD-18co myofibroblasts were first grown on the
241 basolateral side of the polyester Snapwell insert before seeding the IECs on the apical
242 side (multilayer model, Fig. 6A). Furthermore, to recreate the highly porous architecture
243 of the ECM in the basement membrane, epithelial and fibroblasts cells were grown
244 apically and basolaterally respectively on inserts containing electrospun nanofiber
245 scaffolds generated from polyethylene terephthalate to develop a 3-D gut epithelium as
246 reported previously (26). Scanning electron microscopy revealed that these scaffolds

247 exhibited a uniform nanofibrous matrix (Fig. 6B) that supported the attachment and
248 proliferation of Caco-2 cells to form a confluent monolayer (Fig. 6C) and enabled the
249 proliferation of the CCD-18co cells (Fig. 6D).
250
251 Interestingly, in the multilayer model, we find that after infection for 3h and 24h, higher
252 numbers of bacteria adhered to the IECs at both time points compared to the monolayer
253 model without fibroblasts (Fig. 7A). Anti-fibronectin staining of the basolateral side of the
254 membrane containing the fibroblast cells indicated likely degradation of fibronectin and
255 damage to the fibroblast layer at 24h p.i. (Fig. 7B). As before, immunofluorescent
256 staining showed the localisation of *C. difficile* on the epithelial cells at 3h and 24h p.i.
257 (Fig. 7C).
258
259 Similar to the multilayer model, we observed increased adhesion of *C. difficile* to the
260 IECs at 3h and 24h p.i. in the 3-D gut epithelium (Fig. 7D). Similarly, anti-fibronectin
261 staining showed the impaired fibroblast layer in the 3-D model (Fig. 7E). Confocal
262 microscopy revealed the presence of numerous *C. difficile* colonies on the IECs at 24h
263 p.i. (Fig. 7F). Interestingly, at 24h p.i., immunofluorescent staining showed the presence
264 of filamenting *C. difficile* (Fig. 7F), much earlier than seen in the monolayer infection
265 model.
266
267 **A stronger chemokine response to *C. difficile* in the presence of fibroblasts**
268 In both the multilayer and the 3-D models of infection, spores were found to adhere to
269 the epithelium and were present in higher numbers in the apical supernatant, at levels
270 comparable to the 2-D monolayer model (Fig 8A, B). Although there was higher

271 variability, levels of toxin A in the apical supernatants from both models were slightly
272 lower and showed distinct toxin production profiles compared with the 2-D models.
273 Furthermore, we measured levels of toxin B in the 3-D model and were even lower than
274 that observed for toxin A (Figure 8C). Notably, higher levels of IL-8 were stimulated by
275 *C. difficile* infection from the 3-D model (Figure 8D), suggesting a potential role for the
276 myofibroblasts in modulating the *C. difficile* response.
277

278 **DISCUSSION**

279 Attachment to the intestinal mucosa and subsequent multiplication and penetration of
280 the gut epithelium by a pathogen is generally essential for the establishment of a
281 successful infection. We report here the development of *in vitro* human gut models for
282 studying interactions of obligate anaerobes with the host gut epithelium. For the first
283 time, we have modeled prolonged *C. difficile* infection in an *in vitro* human gut mimic.
284 Along with demonstrating *C. difficile* micro-communities, we report formation of *C.*
285 *difficile* filaments, a potential adaptation mechanism during infection.
286

287 Previous *in vitro* infection models have shown the attachment of *C. difficile* on IECs
288 either using conditions that are not appropriate for the bacterium (such as growing in
289 aerobic conditions) or that are limited to short term infection due to the anaerobic growth
290 requirements of *C. difficile* (21, 25, 37). However, in order to study host-pathogen
291 interactions at a molecular and cellular level, precise environmental control and longer
292 scales of infection are essential. The monolayer gut epithelial model described here is
293 ideal for investigating molecular mechanisms underlying *C. difficile*-epithelial

294 interactions as it offers the ability to make cellular, immunological and molecular
295 measurements along with easy substitution of knockout cell lines and introduction of
296 additional cellular components like immune cells.
297
298 Filamentation, a process where bacterial cells continue to elongate without division, is
299 caused in response to environmental or host stress as a way of adaptation and survival
300 (38). For example, uropathogenic *E. coli* in bladder epithelial cells subvert innate
301 immune responses by forming filaments, which evade being phagocytosed by
302 neutrophils (39). Our findings indicate that *C. difficile* filamentation may serve as a
303 mechanism of persistence in the human host. Filamentation may be associated with
304 host cell contact and infection, as preliminary studies indicate that incubation in similar
305 conditions in the absence of cells does not appear to induce this phenotype. Previous
306 studies demonstrated that *Burkholderia pseudomallei* forms filaments when exposed to
307 B-lactam antibiotics to evade killing by the antibiotics (40). Similarly, in *E. coli*, an SOS
308 response occurs when exposed to β-lactams or fluoroquinolones leading to the
309 formation of multinucleated filaments (41). It may be that *in vivo*, *C. difficile* form
310 filaments to avoid being killed by antibiotics but more studies are needed to confirm this
311 and the mechanisms underlying *C. difficile* filament formation.
312
313 Production of spores was observed at 24h and 48h p.i. indicating that spore formation is
314 a key feature of *C. difficile* infection of the gut epithelium, as reported previously using
315 mouse models (42). Previous work showed that *C. difficile* spores adhere to
316 undifferentiated Caco-2 cells after 1h of infection as determined by viable spore counts

317 and fluorescence microscopy (37). Interestingly, we detected similar numbers of spores
318 in the cell-associated bacterial fraction and in the apical supernatants in both the
319 epithelial monolayer and the multilayer/3-D models, suggesting that a high number of
320 the spores formed adhere to the epithelium. This may further indicate that adhesion of
321 spores to the gut mucosa is an inherent feature of *C. difficile* infection.
322
323 Toxin production by *C. difficile* is known to play a role in pathogenesis by disrupting the
324 barrier integrity of the intestinal epithelium leading to increased permeability and re-
325 organization of actin (8). Previous work showed that there was no significant difference
326 in adherence of *C. difficile* (strains R20291 and 630) and their respective toxin mutants
327 (tcdA and tcdB) to the IECs (25). Our data indicate that a strain lacking the major toxins
328 A, B and the binary toxin also does not differ in cell adhesion. Strikingly, the absence of
329 all toxins did not abrogate the increased permeability of the epithelium seen during
330 infection. While there appeared to be a slower decrease in permeability for the triple
331 toxin mutant, ΔABCDTa (Fig. 4B), epithelial integrity was reduced to a level comparable
332 to the WT by 24h p.i. These data suggest that in addition to the main toxins, secreted
333 enzymes or other factors produced by *C. difficile* and bacterial adhesion *per se* via cell
334 surface proteins to the host cells, may contribute to bacterial invasion of the gut
335 epithelium. Further studies on *C. difficile* surface factors and secreted proteins in a toxin
336 negative strain background are required to clarify this.
337
338 The human gut microbiota is dominated by the Firmicutes and Bacteroidetes, which are
339 known to play a role in health and disease (43, 44). As >90% of the bacteria inhabiting

340 the gut are obligate anaerobes, little is known about the adhesion properties of
341 individual bacteria to the intestinal epithelium. Previous research on *Bacteroides fragilis*,
342 a dominant bacterium isolated from intestinal tract infections showed that bile salts
343 enhance the adhesion to the intestinal epithelium and biofilm formation (45). However,
344 for other dominant members of the Bacteroidetes phylum, there is insufficient data as to
345 how they interact with the gut epithelium. Our studies with *B. dorei*, a common gut
346 anaerobe in healthy individuals, demonstrates bacterial adhesion and multiplication on
347 IECs, and validates the utility of this *in vitro* model in studying host cell interactions of
348 other anaerobic gut bacteria.
349
350 While the gut microbiota is known to protect against *C. difficile* infection (2), the direct
351 interactions between commensals and gut pathogens have been poorly understood.
352 Although many genome sequencing studies have associated members of the
353 Bacteroidetes with healthy status, the roles of individual *Bacteroides* species in the gut
354 remains unclear (46-48). Recently, it was shown that *Bacteroides ovatus* inhibited *C.*
355 *difficile* growth in the presence of bile acids (49). In this study we demonstrate
356 suppression of gut cell-associated *C. difficile* by *B. dorei*, in the absence of bile acids
357 and in a physiologically relevant setting. In addition to host-pathogen interactions, the
358 models developed in this work allow three-way interaction studies between
359 commensals, pathogens and the host, i.e. the role of commensals in modulating effects
360 of pathogenic bacteria on the human host. Additionally, as these results may also
361 suggest the potential of non-spore forming anaerobic bacteria in suppressing *C. difficile*

362 growth, such *in vitro* tools may have value in screening and developing novel microbial
363 therapies for treatment of *C. difficile* and other anaerobic infections.
364
365 Three-dimensional models are known to promote more *in vivo*-like cell proliferation,
366 growth differentiation and cell-to cell contact (27). Nanofiber scaffolds, which create a
367 porous architecture similar to the basement membrane underlying the gut epithelium,
368 along with myofibroblast cells in the basal layer, form an excellent mimic of the intestinal
369 epithelium. Morris *et al* showed that nanofibers were beneficial for epithelial cell
370 differentiation but not penetrable to fibroblasts (26). In addition to producing an ECM
371 which provides structural and biochemical support to cells, fibroblasts are also known to
372 produce chemokines when activated by infectious microorganisms such as bacteria
373 (29). Thus, the increased amount of the chemokine IL-8 observed in the 3-D model
374 could be attributed to the myofibroblasts, also as the presence of myofibroblasts is the
375 only difference between the multilayer/3-D models and the monolayer model. Thus, the
376 myofibroblasts may be important in responding to *C. difficile* infection. In addition, the
377 increased *C. difficile* adhesion observed in the multilayer and the 3-D models, which
378 presumably leads to quicker progressing infection, could also be the result of indirect
379 modulation of the epithelial barrier by the myofibroblast cells. Both the multilayer and 3-
380 D gut models have huge potential in studying *C. difficile* pathogenesis, particularly for
381 investigating host invasion and interactions with basolateral surface of the host
382 epithelium and are currently being utilized for studying functions of secreted *C. difficile*
383 factors in the laboratory.
384

385 Overall, we have developed highly useful tools for studying *C. difficile* host-interactions
386 which we expect to have broad applications in studying anaerobic gut commensals and
387 their interactions with pathogens and the host.
388

389 **MATERIALS AND METHODS**

390 *Bacterial strains used and growth conditions*

391 *C. difficile* R20291 was cultured on brain heart infusion agar (Sigma-Aldrich, UK)
392 supplemented with 1 g/L cysteine (Sigma-Aldrich, UK), 5 g/L yeast extract (BHIS) under
393 anaerobic conditions (80% N_2, 10% CO_2, 10% H_2) in a Don Whitley workstation
394 (Yorkshire, UK). The triple toxin mutant, R20291 *tcd*A *tcd*B *cdt*A ($A^-B^-CDTa^-$), a kind gift
395 from Sarah Kuehne and Nigel Minton (36) was cultured in the same media as the WT
396 strain supplemented with lincomycin hydrochloride (Sigma-Aldrich, UK).
397

398 *Cell culture*

399 Intestinal epithelial cell line, Caco-2 (P6-P21) from American Type Culture Collection,
400 mucus producing cell line, HT29-MTX (P45-P56), gift from Nathalie Juge and fibroblast
401 cells, CCD-18co (P10-P17) were used. Caco-2 cells were grown in Dulbecco's Modified
402 Eagle Medium (DMEM) supplemented with 10% fetal bovine serum (FBS) and 1%
403 penicillin-streptomycin. HT29-MTX was grown in DMEM and CCD-18co in Eagle's
404 Minimum Essential Medium media. Both media were supplemented with 10% FBS, 1%
405 penicillin-streptomycin, 2 mM glutamine and 1% non-essential amino acids (Sigma-
406 Aldrich, UK). All cell lines were maintained in 5% CO_2 in a humidified incubator at 37°C.
407

408 For the epithelial 2-D models, Caco-2 and HT29-MTX were mixed in a 9:1 ratio and 2 x
409 10^5 cells/mL were seeded on a 12 mm Snapwell inserts (tissue culture treated polyester
410 membrane, Corning, New York, USA) supported by a detachable ring for 2 weeks to
411 form a polarized monolayer. For the multilayer and 3-D models, CCD-18co (1 X10^4
412 cells/ml) were first seeded on the basolateral layer of the polyester Snapwell insert or
413 electrospun nanofiber scaffold for 5 days after which Caco-2 and HT29-MTX were
414 seeded on the apical side as in the 2-D models for 14 days. Prior to the infection
415 experiments, the cell culture medium in the Snapwell inserts was replaced with
416 antibiotic-free medium.
417
418 *Vertical diffusion chamber set up and measurement of transepithelial electrical*
419 *resistance*
420 The Snapwell inserts containing the polarized cell layer were placed between the two
421 half chambers of the vertical diffusion chamber (Harvard Apparatus, Cambridge, UK)
422 and sealed with the provided clamps. DMEM with 10% FBS was placed on both sides of
423 the chamber. Transepithelial electrical resistance measurements was performed using
424 Harvard/Navicyte electrodes on the EC-800 Epithelial Voltage Clamp (Harvard
425 Apparatus, Cambridge, UK) over 24h.
426
427 *Infection of intestinal epithelial cells (IECs)*
428 A single bacterial colony was inoculated in pre-reduced BHI broth (Oxoid)
429 supplemented with 1 g/L cysteine (Sigma-Aldrich, UK) and 5 g/L yeast extract and
430 incubated at 37 ^{o}C overnight. The culture was centrifuged at 10,000g for 5 mins

431 (Eppendorf 5810R) and bacterial pellet was resuspended in DMEM supplemented with
432 10% FBS and incubated at 37 ^{o}C for at least an hour. This culture was used to infect the
433 IECs at a predetermined MOI of 100:1 in the apical side of the VDC containing the
434 IECs. The apical chamber was diffused with anaerobic gas mixture (10% CO_2, 10% H_2,
435 80% N_2, BOC, UK) and the basolateral compartment with 5% CO_2 and 95% air (BOC,
436 UK). At 3h p.i., the apical media containing the *C. difficile* was removed, the IECs
437 washed in PBS and prereduced DMEM with 10% FBS added. It was incubated for a
438 further 3h or up to 24h. The apical and basolateral media was then removed and stored
439 at -80 ^{o}C. The IECs were washed thrice in PBS before lysing in sterile water. Serial
440 dilutions were performed and plated on appropriate plates to determine the number of
441 cell-associated bacteria. To determine spore production, the lysed cells and apical
442 supernatants were heat treated at 65°C for 20 mins, serial dilututed and plated on BHI
443 agar supplemented with 0.1% sodium taurocholate (Sigma-Aldrich, UK).
444
445 For the co-culture experiments with *B. dorei*, the same protocol was followed except
446 that both strains were grown in Schaedler anaerobic broth (Oxoid, UK) overnight and an
447 MOI of 1000: 1 was used. To differentiate *C. difficile* colonies from *B. dorei*, the BHIS
448 agar was supplemented with *C. difficile* selective supplement (Oxoid, UK).
449
450 *ELISA assays*
451 *C. difficile* toxin production was determined by ELISA following the manufacturer's
452 instructions (tgcBIOMICS, Bingen am Rhein, Germany). IL-8 production was also

453 determined by analysis of basolateral supertants from VDC's using a human IL-8 ELISA
454 kit (R&D systems, Minneapolis, USA).
455
456 *Electrospinning protocol*
457 Electrospinning procedure was performed as described previously (26). Briefly,
458 scaffolds were produced by dissolving polyethylene terephthalate (PET, from food
459 grade drinking bottles) in equal ratio of trifluoroacetic acid and dichloromethane (1:1) to
460 create a 10% (w/v) PET solution to produce the nanofiber scaffolds. Electrospinning
461 processing parameters included an applied voltage of 14kV, a tip-collector distance
462 (TCD) of 15cm, a flow rate of 0.5 mL/h and an 18 gauge spinneret for a period of 2h.
463 Electrospinning was conducted at ambient conditions in a ducted fume hood with fibers
464 collected on a stainless steel rotating drum (50 rpm). Once collected, the scaffolds were
465 stored in aluminum foil at room temperature until required. Prior to cell culture,
466 scaffolds were positioned in 12 mm Snapwell inserts (Corning, New York, USA) by
467 replacing the commercial membrane with the electrospun nanofiber matrix. PET
468 scaffolds were cut into 2.5 cm diameter circles and fixed with Costar Snapwell
469
470 inserts using aquarium sealant glue (King British, Beaphar Company). They were
471 sterilized by exposing to UV at the power of 80 mJ/cm2 for 15 minutes on each side
472 using a UV lamp (CL-1000 Ultraviolet Crosslinker) and soaking in 10x antibiotic-
473 antimycotic solution (final concentration: 1,000 units/mL penicillin, 1 mg/mL
474 streptomycin and 2.5 µg/mL amphotericin B, Sigma Aldrich, Poole, UK) for 3h at 25 °C.
475 Antibiotic-antimycotic solution was then removed and the scaffolds were washed with

476 PBS (pH 7.4) three times. The scaffolds were air-dried in the microbiological class 2
477 safety cabinet overnight.
478
479 *Scanning Electron Microscopy (SEM)*
480 The fiber morphology of the nanofiber scaffolds was assessed using SEM. Acellular
481 samples were sputter coated (Leica EMSCD005) with gold for 4-5 mins prior to
482 microscopy. Scaffolds seeded with cells were fixed in 3% (v/v) glutaraldehyde overnight
483 at 4°C. Samples were washed thrice in PBS and dehydrated through a series of
484 industrial methylated spirits (IMS) concentrations diluted in water (25-100% *v/v*) for 10
485 mins each. Following dehydration, hexamethyldisilazane (HMDS) was added to
486 chemically dry the samples, this process was then repeated and the samples allowed to
487 air dry overnight before sputter coating as described above. Scaffold and cell
488 morphology was observed at various magnifications as indicated on the scale bar of the
489 images (JEOL JSM-6100, JEOL, UK). Images were processed using ImageJ software
490 (W. Rasband, National Institute of Health, USA) to determine the fiber diameter and 150
491 measurements (50 measurements per scaffold) from 3 independently produced
492 scaffolds were assessed.
493
494 *Immunofluorescence and imaging*
495 The Snapwell inserts, containing either the commercial membrane or PET nanofiber
496 scaffold, were fixed in 4% PFA for 15 min, washed in PBS, permeabilized with 1%
497 saponin (Sigma-Aldrich, UK) in 0.3% triton X-100 (Fisher Scientific, UK) and thereafter
498 blocked against non-specific antibody binding with 3% BSA in PBS (Sigma-Aldrich, UK).

499 For staining *C. difficile*, infected cells were incubated with anti-*C. difficile* serum for 1h,
500 followed by Alexa Fluor 488 goat anti-rabbit secondary antibody (New England Biolabs,
501 UK) for 1h. Alexa fluor phalloidin 647 was used to stain the actin cytoskeleton and cell
502 nuclei were stained with ProLong Gold Antifade mountant containing 4,6-diamidino-2-
503 phenylindole (DAPI) (New England Biolabs, UK). To determine mucus production, the
504 Snapwell inserts were fixed, permeabilized and blocked as described above. The
505 Snapwell insert was incubated with mucin 2 anti-rabbit primary antibody (Santa Cruz
506 Biotechnology, US) overnight at 4°C followed by Alexa Fluor 488 goat anti-rabbit
507 secondary antibody (New England Biolabs, UK) for 1h. Images were taken using a
508 confocal spinning-disk microscope (VOX UltraView, PerkinElmer, UK) with a 40X oil
509 objective and two Hamamatsu ORCA-R2 cameras, by Volocity 6.0 (PerkinElmer, UK).
510 Post-image analysis was performed with ImageJ software.
511
512 *Statistical analysis*
513 Student t test (two tailed) was used to determine the significance between two groups.
514 Significance is represented as *$p < 0.05$, **$p < 0.01$, ***$p < 0.001$ and ****$p< 0.0001$.
515 Except stated otherwise, all the results presented are the average of 3 independent
516 experiments performed in duplicates or triplicates. The error bars indicate the standard
517 deviation (SD).
518
519 **ACKNOWLEDGEMENTS**: This work is funded by the Wellcome Trust Seed Award in
520 Science to MU (grant no 108263/Z/15/Z) and a Synthetic Biology PhD funded by
521 BBSRC & EPSRC, grant number: EP/L016494/1 to JH. This grant was awarded to the

522 Warwick Integrative Synthetic Biology Centre (grant ref: BB/M017982/1) funded under
523 the UK Research Councils' Synthetic Biology for Growth programme. We thank Nigel
524 Minton, Sarah Kuehne and Trevor Lawley for providing *C. difficile* strains and Nathalie
525 Juge for providing the HT29-MTX cell line. We thank Arnaud Kengmo Tchoupa for
526 reading the manuscript.

527

528

529 **REFERENCES**

530

531 1. Adamu BO, Lawley TD. 2013. Bacteriotherapy for the treatment of intestinal
532 dysbiosis caused by *Clostridium difficile* infection. Current Opinion in
533 Microbiology 16:596-601.
534 2. Fuentes S, van Nood E, Tims S, Heikamp-de Jong I, ter Braak CJF, Keller JJ,
535 Zoetendal EG, de Vos WM. 2014. Reset of a critically disturbed microbial
536 ecosystem: faecal transplant in recurrent *Clostridium difficile* infection. The ISME
537 Journal 8:1621-1633.
538 3. Lessa FC, Mu Y, Bamberg WM, Beldavs ZG, Dumyati GK, Dunn JR, Farley MM,
539 Holzbauer SM, Meek JI, Phipps EC. 2015. Burden of *Clostridium difficile* infection
540 in the United States. N Engl J Med 372: 825-834.
541 4. Gravel D, Miller M, Simor A, Taylor G, Gardam M, McGeer A, Hutchinson J,
542 Moore D, Kelly S, Boyd D, Mulvey M. 2009. Health Care-Associated *Clostridium*
543 *difficile* Infection in Adults Admitted to Acute Care Hospitals in Canada: A

544 Canadian Nosocomial Infection Surveillance Program Study. Clinical Infectious
545 Diseases 48:568-576.
546 5. Collins DA, Selvey LA, Celenza A, Riley TV. 2017. Community-associated
547 *Clostridium difficile* infection in emergency department patients in Western
548 Australia. Anaerobe 48:121-125.
549 6. Davies KA, Longshaw CM, Davis GL, Bouza E, Barbut F, Barna Z, Delmée M,
550 Fitzpatrick F, Ivanova K, Kuijper E, Macovei IS, Mentula S, Mastrantonio P, von
551 Müller L, Oleastro M, Petinaki E, Pituch H, Norén T, Nováková E, Nyč O, Rupnik
552 M, Schmid D, Wilcox MH. Underdiagnosis of *Clostridium difficile* across Europe:
553 the European, multicentre, prospective, biannual, point-prevalence study of
554 *Clostridium difficile* infection in hospitalised patients with diarrhoea (EUCLID).
555 The Lancet Infectious Diseases 14:1208-1219.
556 7. Kuehne SA, Cartman ST, Heap JT, Kelly ML, Cockayne A, Minton NP. 2010. The
557 role of toxin A and toxin B in *Clostridium difficile* infection. Nature 467:711-3.
558 8. Aktories K, Schwan C, Jank T. 2017. *Clostridium difficile* Toxin Biology. Annual
559 Review of Microbiology 71:281-307.
560 9. Lyras D, O'Connor JR, Howarth PM, Sambol SP, Carter GP, Phumoonna T,
561 Poon R, Adams V, Vedantam G, Johnson S, Gerding DN, Rood JI. 2009. Toxin B
562 is essential for virulence of *Clostridium difficile*. Nature 458:1176-9.
563 10. Calabi E, Calabi F, Phillips AD, Fairweather NF. 2002. Binding of *Clostridium*
564 *difficile* Surface Layer Proteins to Gastrointestinal Tissues. Infection and
565 Immunity 70:5770-5778.

566 11. Merrigan MM, Venugopal A, Roxas JL, Anwar F, Mallozzi MJ, Roxas BAP,
567 Gerding DN, Viswanathan VK, Vedantam G. 2013. Surface-Layer Protein A
568 (SlpA) Is a Major Contributor to Host-Cell Adherence of *Clostridium difficile*.
569 PLOS ONE 8:e78404.
570 12. Kovacs-Simon A, Leuzzi R, Kasendra M, Minton N, Titball RW, Michell SL. 2014.
571 Lipoprotein CD0873 Is a Novel Adhesin of *Clostridium difficile*. The Journal of
572 Infectious Diseases 210:274-284.
573 13. Barketi-Klai A, Hoys S, Lambert-Bordes S, Collignon A, Kansau I. 2011. Role of
574 fibronectin-binding protein A in *Clostridium difficile* intestinal colonization. Journal
575 of Medical Microbiology 60:1155-1161.
576 14. Hennequin C, Porcheray F, Waligora-Dupriet A-J, Collignon A, Barc M-C,
577 Bourlioux P, Karjalainen T. 2001. GroEL (Hsp60) of *Clostridium difficile* is
578 involved in cell adherence. Microbiology 147:87-96.
579 15. Waligora A-J, Hennequin C, Mullany P, Bourlioux P, Collignon A, Karjalainen T.
580 2001. Characterization of a Cell Surface Protein of *Clostridium difficile* with
581 Adhesive Properties. Infection and Immunity 69:2144-2153.
582 16. Tasteyre A, Barc M-C, Collignon A, Boureau H, Karjalainen T. 2001. Role of FliC
583 and FliD Flagellar Proteins of *Clostridium difficile* in Adherence and Gut
584 Colonization. Infection and Immunity 69:7937-7940.
585 17. Batah J, Kobeissy H, Bui Pham PT, Deneve-Larrazet C, Kuehne S, Collignon A,
586 Janoir-Jouveshomme C, Marvaud JC, Kansau I. 2017. *Clostridium difficile*
587 flagella induce a pro-inflammatory response in intestinal epithelium of mice in
588 cooperation with toxins. Sci Rep 7:3256. doi:10.1038/s41598-017-03621-z.

589 18. Lawley TD, Clare S, Deakin LJ, Goulding D, Yen JL, Raisen C, Brandt C, Lovell
590 J, Cooke F, Clark TG, Dougan G. 2010. Use of Purified *Clostridium difficile*
591 Spores To Facilitate Evaluation of Health Care Disinfection Regimens. Applied
592 and Environmental Microbiology 76:6895-6900.
593 19. Vohra P, Poxton IR. 2011. Efficacy of decontaminants and disinfectants against
594 *Clostridium difficile*. Journal of Medical Microbiology 60:1218-1224.
595 20. Janvilisri T, Scaria J, Chang Y-F. 2010. Transcriptional profiling of *Clostridium*
596 *difficile* and Caco-2 cells during infection. The Journal of infectious diseases
597 202:282-290.
598 21. Cerquetti M, Serafino A, Sebastianelli A, Mastrantonio P. 2002. Binding of
599 *Clostridium difficile* to Caco-2 epithelial cell line and to extracellular matrix
600 proteins. FEMS Immunology & Medical Microbiology 32:211-218.
601 22. Mora-Uribe P, Miranda-Cárdenas C, Castro-Córdova P, Gil F, Calderón I,
602 Fuentes JA, Rodas PI, Banawas S, Sarker MR, Paredes-Sabja D. 2016.
603 Characterization of the Adherence of *Clostridium difficile* Spores: The Integrity of
604 the Outermost Layer Affects Adherence Properties of Spores of the Epidemic
605 Strain R20291 to Components of the Intestinal Mucosa. Frontiers in Cellular and
606 Infection Microbiology 6:99. doi: 10.3389/fcimb.2016.00099.
607 23. Schüller S, Phillips AD. 2010. Microaerobic conditions enhance type III secretion
608 and adherence of enterohaemorrhagic *Escherichia coli* to polarized human
609 intestinal epithelial cells. Environmental Microbiology 12:2426-2435.
610 24. Mills DC, Gundogdu O, Elmi A, Bajaj-Elliott M, Taylor PW, Wren BW, Dorrell N.
611 2012. Increase in *Campylobacter jejuni* invasion of intestinal epithelial cells under

612 low-oxygen coculture conditions that reflect the *in vivo* environment. Infection and
613 Immunity 80:1690-1698.
614 25. Jafari NV, Kuehne SA, Minton NP, Allan E, Bajaj-Elliott M. 2016. *Clostridium*
615 *difficile*-mediated effects on human intestinal epithelia: Modelling host-pathogen
616 interactions in a vertical diffusion chamber. Anaerobe 37:96-102.
617 26. Morris GE, Bridge JC, Brace LA, Knox AJ, Aylott JW, Brightling CE,
618 Ghaemmaghami AM, Rose FR. 2014. A novel electrospun biphasic scaffold
619 provides optimal three-dimensional topography for *in vitro* co-culture of airway
620 epithelial and fibroblast cells. Biofabrication 6:035014.
621 27. Kook Y-M, Jeong Y, Lee K, Koh W-G. 2017. Design of biomimetic cellular
622 scaffolds for co-culture system and their application. Journal of Tissue
623 Engineering 8:2041731417724640.
624 28. Ravi M, Paramesh V, Kaviya SR, Anuradha E, Solomon FDP. 2015. 3D Cell
625 Culture Systems: Advantages and Applications. Journal of Cellular Physiology
626 230:16-26.
627 29. Smith RS, Smith TJ, Blieden TM, Phipps RP. 1997. Fibroblasts as sentinel cells.
628 Synthesis of chemokines and regulation of inflammation. The American Journal
629 of Pathology 151:317-322.
630 30. Kasendra M, Barrile R, Leuzzi R, Soriani M. 2014. *Clostridium difficile* Toxins
631 Facilitate Bacterial Colonization by Modulating the Fence and Gate Function of
632 Colonic Epithelium. Journal of Infectious Diseases 209:1095-1104.
633 31. Leslie JL, Huang S, Opp JS, Nagy MS, Kobayashi M, Young VB, Spence JR.
634 2015. Persistence and Toxin Production by *Clostridium difficile* within Human

635 Intestinal Organoids Result in Disruption of Epithelial Paracellular Barrier
636 Function. Infection and Immunity 83:138-145.
637 32. Barrila J, Yang J, Crabbé A, Sarker SF, Liu Y, Ott CM, Nelman-Gonzalez MA,
638 Clemett SJ, Nydam SD, Forsyth RJ, Davis RR, Crucian BE, Quiriarte H, Roland
639 KL, Brenneman K, Sams C, Loscher C, Nickerson CA. 2017. Three-dimensional
640 organotypic co-culture model of intestinal epithelial cells and macrophages to
641 study *Salmonella enterica* colonization patterns. npj Microgravity 3:10.
642 33. DeCicco RePass MA, Chen Y, Lin Y, Zhou W, Kaplan DL, Ward HD. 2017. Novel
643 Bioengineered Three-Dimensional Human Intestinal Model for Long-Term
644 Infection of *Cryptosporidium parvum*. Infection and Immunity 85:e00731-16.
645 34. Drummond CG, Nickerson CA, Coyne CB. 2016. A Three-Dimensional Cell
646 Culture Model To Study Enterovirus Infection of Polarized Intestinal Epithelial
647 Cells. mSphere 1. doi: 10.1128/mSphere.00030-15.
648 35. Rao K, Erb-Downward JR, Walk ST, Micic D, Falkowski N, Santhosh K, Mogle
649 JA, Ring C, Young VB, Huffnagle GB. 2014. The systemic inflammatory
650 response to *Clostridium difficile* infection. PLoS One 9:e92578.
651 36. Kuehne SA, Collery MM, Kelly ML, Cartman ST, Cockayne A, Minton NP. 2013.
652 Importance of toxin A, toxin B, and CDT in virulence of an epidemic *Clostridium*
653 *difficile* strain. The Journal of Infectious Diseases 209:83-86.
654 37. Paredes-Sabja D, Sarker MR. 2012. Adherence of *Clostridium difficile* spores to
655 Caco-2 cells in culture. Journal of Medical Microbiology 61:1208-1218.
656 38. Justice SS, Hunstad DA, Cegelski L, Hultgren SJ. 2008. Morphological plasticity
657 as a bacterial survival strategy. Nat Rev Micro 6:162-168.

658 39. Justice SS, Hunstad DA, Seed PC, Hultgren SJ. 2006. Filamentation by
659 *Escherichia coli* subverts innate defenses during urinary tract infection.
660 Proceedings of the National Academy of Sciences 103:19884-19889.
661 40. Jones AL, Beveridge TJ, Woods DE. 1996. Intracellular survival of *Burkholderia*
662 *pseudomallei*. Infection and Immunity 64:782-790.
663 41. Miller C, Thomsen LE, Gaggero C, Mosseri R, Ingmer H, Cohen SN. 2004. SOS
664 response induction by ß-lactams and bacterial defense against antibiotic lethality.
665 Science 305:1629-1631.
666 42. Deakin LJ, Clare S, Fagan RP, Dawson LF, Pickard DJ, West MR, Wren BW,
667 Fairweather NF, Dougan G, Lawley TD. 2012. The *Clostridium difficile* spo0A
668 Gene Is a Persistence and Transmission Factor. Infection and Immunity 80:2704-
669 2711.
670 43. Browne HP, Forster SC, Anonye BO, Kumar N, Neville BA, Stares MD, Goulding
671 D, Lawley TD. 2016. Culturing of 'unculturable'human microbiota reveals novel
672 taxa and extensive sporulation. Nature 533:543-546.
673 44. Lozupone CA, Stombaugh JI, Gordon JI, Jansson JK, Knight R. 2012. Diversity,
674 stability and resilience of the human gut microbiota. Nature 489:220-230.
675 45. Pumbwe L, Skilbeck CA, Nakano V, Avila-Campos MJ, Piazza RMF, Wexler HM.
676 2007. Bile salts enhance bacterial co-aggregation, bacterial-intestinal epithelial
677 cell adhesion, biofilm formation and antimicrobial resistance of Bacteroides
678 fragilis. Microbial Pathogenesis 43:78-87.

679 46. Qin J, Li R, Raes J, Arumugam M, Burgdorf KS, Manichanh C, Nielsen T, Pons
680 N, Levenez F, Yamada T. 2010. A human gut microbial gene catalogue
681 established by metagenomic sequencing. nature 464:59-65.
682 47. Consortium HMP. 2012. Structure, function and diversity of the healthy human
683 microbiome. Nature 486:207-214.
684 48. Lloyd-Price J, Abu-Ali G, Huttenhower C. 2016. The healthy human microbiome.
685 Genome Medicine 8: 51. doi: 10.1186/s13073-016-0307-y.
686 49. Yoon S, Yu J, McDowell A, Kim SH, You HJ, Ko G. 2017. Bile salt hydrolase-
687 mediated inhibitory effect of Bacteroides ovatus on growth of Clostridium difficile.
688 Journal of Microbiology 55:892-899.
689

690 **Figure legends**

691 **FIG 1**. **Scheme for generation of epithelial layers for use within vertical diffusion**
692 **chambers**. For the 2-D model, intestinal epithelial cells were grown to form a polarized
693 confluent monolayer in a Snapwell filter for 2 weeks before inserting in the VDCs. *C.*
694 *difficile* was added to the apical chamber which is perfused with an anaerobic gas mix
695 and incubated for different times while maintaining anaerobic conditions. The
696 basolateral compartment was perfused with a mixture of 5% CO_2 and 95% air,
697 necessary for growth of IECs.
698

699 **FIG 2**. **The VDC permits growth of host cells and enables *C. difficile* to adhere and**
700 **multiply on gut epithelial cells.** (A) Reduction in TEER measurements after infection
701 indicating increasing permeability compared to uninfected controls, $^{**}p < 0.01$ as

702 determined by two tailed student t test. (B) Immunofluorescent microscopy images of
703 uninfected controls at 24h and 48h. Actin is stained with phalloidin (red) and cell nuclei
704 are stained with DAPI (blue), Scale bar =10 μM. (C) Colony counts from infected cells to
705 determine the number of adherent or cell-associated bacteria. A significant increase in
706 adherent *C. difficile* is observed as infection progresses. Data is representative of mean
707 of 3 independent experiments and error bars indicate SD, ***$p < 0.001$ and ****$p<$
708 0.0001 (D) Immunofluorescent microscopy images of *C. difficile* infected IECs at 6h,
709 24h and 48h p.i. showing colocalization of the bacteria, stained with anti *C. difficile*
710 antibodies (green) with actin, stained with phalloidin (red). Cell nuclei are stained with
711 DAPI (blue). Reorganization and destruction of actin filaments is observed at 24h and
712 48h p.i. Micro-communities formed at 24h p.i, and *C. difficile* filamentous forms,
713 observed at 48h p.i. are indicated by arrows. Scale bar =10 μM. Inset shows the
714 orthogonal XZ axis view of the IECs.
715
716 **FIG 3. Production of *C. difficile* spores, toxins and host responses to infection.** (A)
717 Colony counts of spores recovered after heat treatment of the adherent *C. difficile*
718 fraction and the apical supernatants in the 2-D epithelial model (B) ELISA for *C. difficile*
719 toxin A shows increased toxin after extended infection (C). ELISA for human IL-8
720 indicates increased IL-8 production at 24h and 48h p.i.
721
722 **FIG 4. *C. difficile* toxins are not required for adherence to gut epithelial cells** (A)
723 Colony counts from epithelial cells infected with the WT R20291 and triple toxin mutant
724 ($A^-B^-CDTa^-$) demonstrates that absence of the toxins does not affect adherence to the

725 IECs (ns, not significant) (B) TEER values showing reduction at 24h p.i. between the
726 WT and the triple toxin mutant. (C) Representative confocal microscopy images of IECs
727 infected with the triple toxin mutant at 24h p.i. showing less redistribution of actin,
728 stained with phalloidin (red) as compared to the WT. Inset shows the orthogonal XZ axis
729 view of the IECs. *C. difficile* is stained green, actin, red and cell nuclei, blue, Scale bar =
730 10 μM.
731
732 **FIG. 5. Studying *C. difficile*-commensal interactions within epithelial models.** (A)
733 Co–culture studies of *B. dorei* with *C. difficile* in the VDC showed no significant inhibition
734 at 3h p.i. (B) However, at 24h, a significant inhibition of *C. difficile* is observed. Co-
735 culture Bd and Cd represents the growth of *B. dorei* and *C. difficile* respectively in the
736 mixed culture (Bd, *B. dorei* and Cd, *C. difficile*). ***$p < 0.001$.
737
738 **FIG 6. Scheme for generation of multilayer and 3-D models containing fibroblast**
739 **cells and cell growth on the electrospun nanofibrous matrix** (A) Fibroblast cells
740 were first seeded on the basolateral side of the Snapwell or nanofiber scaffold for the
741 multilayer and 3-D models for 5 days. Thereafter, IECs were cultured on the apical side
742 for 2 weeks before placing the Snapwell filter between two halves of the chamber. *C.*
743 *difficile* was infected apically while maintaining anaerobic conditions and the basolateral
744 compartment was perfused with 5% CO_2 and 95% air. (B) Polyethylene terephthalate
745 (PET; 10% *w/v*) was electrospun and exhibited a uniform nanofibrous matrix as
746 determined by scanning electron microscopy. (C) Caco-2 epithelial cells were able to
747 form a confluent monolayer on the nanofibrous scaffolds (the scaffold can be seen

748 underneath the cells following processing for SEM). (D) The CCD-18co cells proliferated
749 across the nanofibrous scaffold forming cell processes to adhere to the nanofibers.
750
751 **FIG 7. Infection of *C. difficile* in multilayer and 3-D model leads to increased**
752 **adhesion.** Increased adherence of *C. difficile* in the multilayer and 3-D models, where
753 fibroblasts are grown as a basolateral layer on polyester and nanofibers respectively.
754 (A) Serial dilutions of the infected epithelial cell lysates were plated to determine the
755 number of cell-associated bacteria in the multilayer model. (B) Anti-fibronectin (green)
756 staining of fibroblast cells in the basolateral layer of the control and infected cells at 24h
757 p.i showing degradation of the fibroblast layer in the multilayer model. (C)
758 Representative images of *C. difficile* on the apical layer at 3h and 24h p.i. Inset shows
759 the orthogonal XZ axis view of the IECs. *C. difficile* is stained green, actin, red and cell
760 nuclei, blue, Scale bar = 10 μM. (D) *C. difficile* colony counts from infected cells in the 3-
761 D model (E) Anti-fibronectin (green) staining of fibroblast cells in the basolateral layer at
762 24h p.i. (F) Immunofluorescent microscopy images of *C. difficile* infected IECs at 3h and
763 24h p.i in the 3-D model. *C. difficile* filamentous forms are observed at 24h p.i.
764 (indicated by arrows). Inset shows the orthogonal XZ axis view of the IECs. *C. difficile* is
765 stained green, actin, red and cell nuclei, blue, Scale bar = 10 μM.
766
767 **FIG 8. *C. difficile* spores and toxin production, and host response to infection in**
768 **the multilayer and 3-D models.** Colony counts of spores in the cell-associated *C.*
769 *difficile* fraction and the apical supernatants in the (A) multilayer and (B) 3-D model. (C)
770 Toxin A and B levels in the multilayer and 3-D model. (D) IL-8 levels are significantly
771 increased in the 3-D model at 24h p.i., $^{**}p < 0.01$ as determined by the student t test.

772

773 **FIG. S1. Characterization of mucus production in the Caco-2/HT29-MTX**
774 **monolayer.** Immunofluorescent microscopy images of Caco2/HT29-MTX monolayer
775 stained with mucin 2 antibody showing mucus production (green) after 14 days of
776 growth. Actin is stained red and cell nuclei, blue. Inset shows the orthogonal XZ axis
777 view of the IECs. Scale bar = 10 μM.

778

779 **FIG. S2. The vertical diffusion chamber maintains anaerobic conditions.** *C. difficile*
780 was grown in the VDC or anaerobic chamber for 3h and serial dilutions of the apical
781 supernatant were plated to enumerate colony counts (ns, not significant as determined
782 by students t-test).

783

784 **FIG S3. Fiber diameter of the electrospun nanofibrous matrix.** Fiber diameter
785 analysis revealed that the average fiber diameter was 457 ± 170 nm, with fibers in the
786 range of 200-1100 nm (n=150 measurements, 50 measurements per scaffold from 3
787 independently produced scaffolds).

788

789

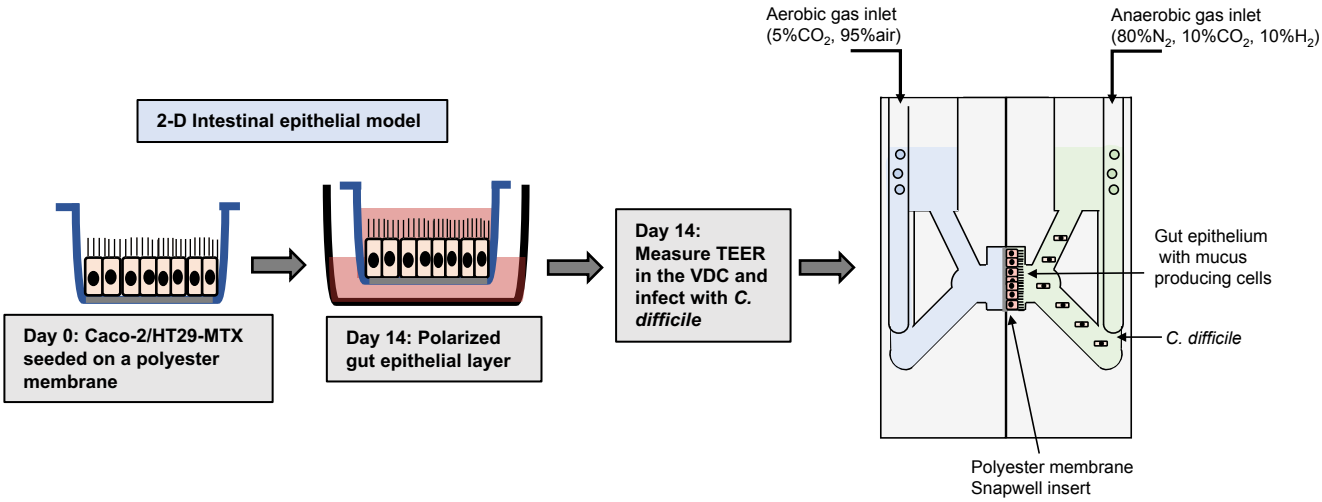

FIG 1. **Scheme for generation of epithelial layers for use within vertical diffusion chambers**. For the 2-D model, intestinal epithelial cells were grown to form a polarized confluent monolayer in a Snapwell filter for 2 weeks before inserting in the VDCs. *C. difficile* was added to the apical chamber which is perfused with an anaerobic gas mix and incubated for different times while maintaining anaerobic conditions. The basolateral compartment was perfused with a mixture of 5% CO_2 and 95% air, necessary for growth of IECs.

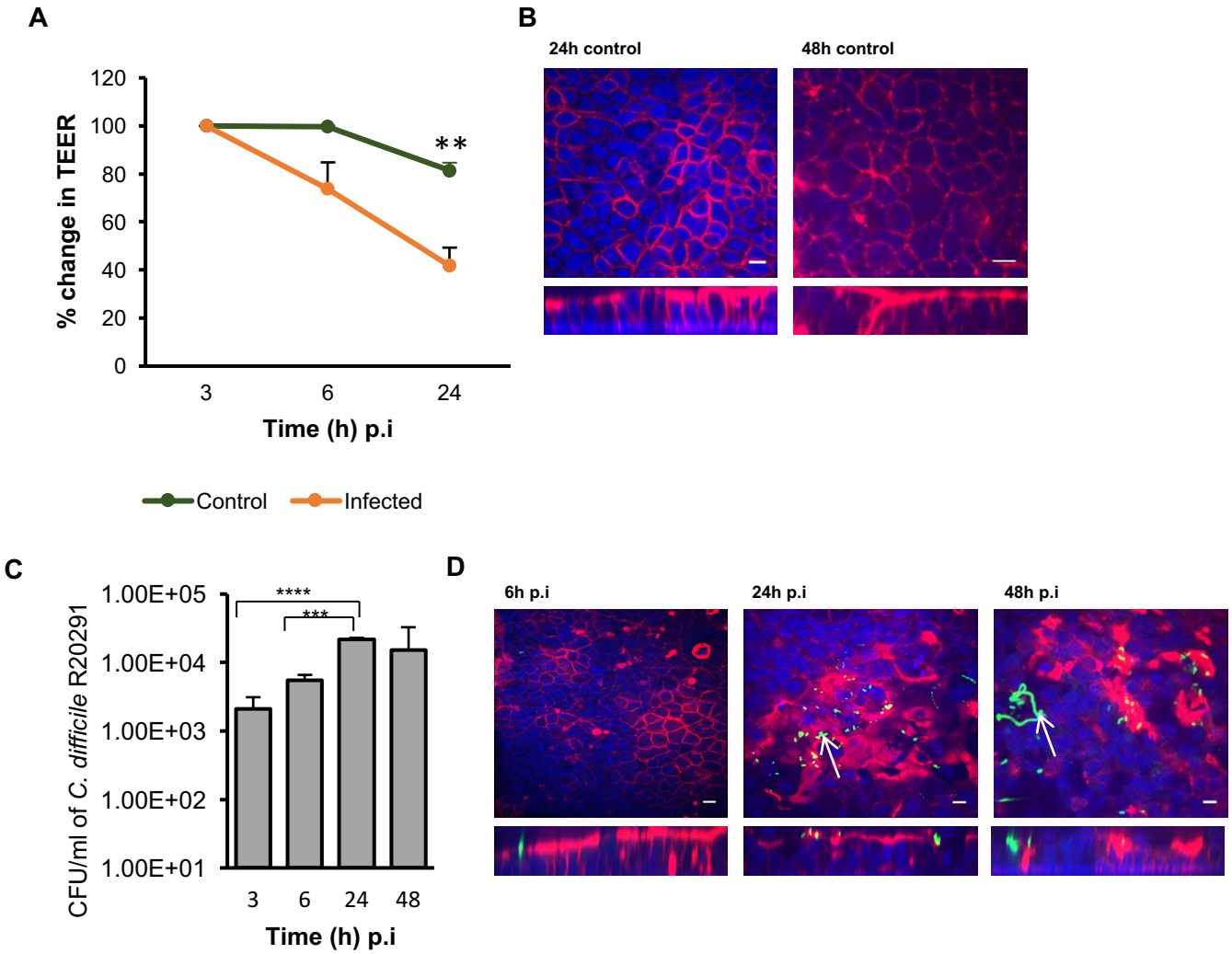

FIG 2. The VDC permits growth of host cells and enables *C. difficile* to adhere and multiply on gut epithelial cells. (A) Reduction in TEER measurements after infection indicating increasing permeability compared to uninfected controls, **$p < 0.01$ as determined by two tailed student t test. (B) Immunofluorescent microscopy images of uninfected controls at 24h and 48h. Actin is stained with phalloidin (red) and cell nuclei are stained with DAPI (blue), Scale bar =10 μM. (C) Colony counts from infected cells to determine the number of adherent or cell-associated bacteria. A significant increase in adherent *C. difficile* is observed as infection progresses. Data is representative of mean of 3 independent experiments and error bars indicate SD, ***$p < 0.001$ and ****$p < 0.0001$ (D) Immunofluorescent microscopy images of *C. difficile* infected IECs at 6h, 24h and 48h p.i. showing colocalization of the bacteria, stained with anti *C. difficile* antibodies (green) with actin, stained with phalloidin (red). Cell nuclei are stained with DAPI (blue). Reorganization and destruction of actin filaments is observed at 24h and 48h p.i. Micro-communities formed at 24h p.i, and *C. difficile* filamentous forms, observed at 48h p.i. are indicated by arrows. Scale bar =10 μM. Inset shows the orthogonal XZ axis view of the IECs.

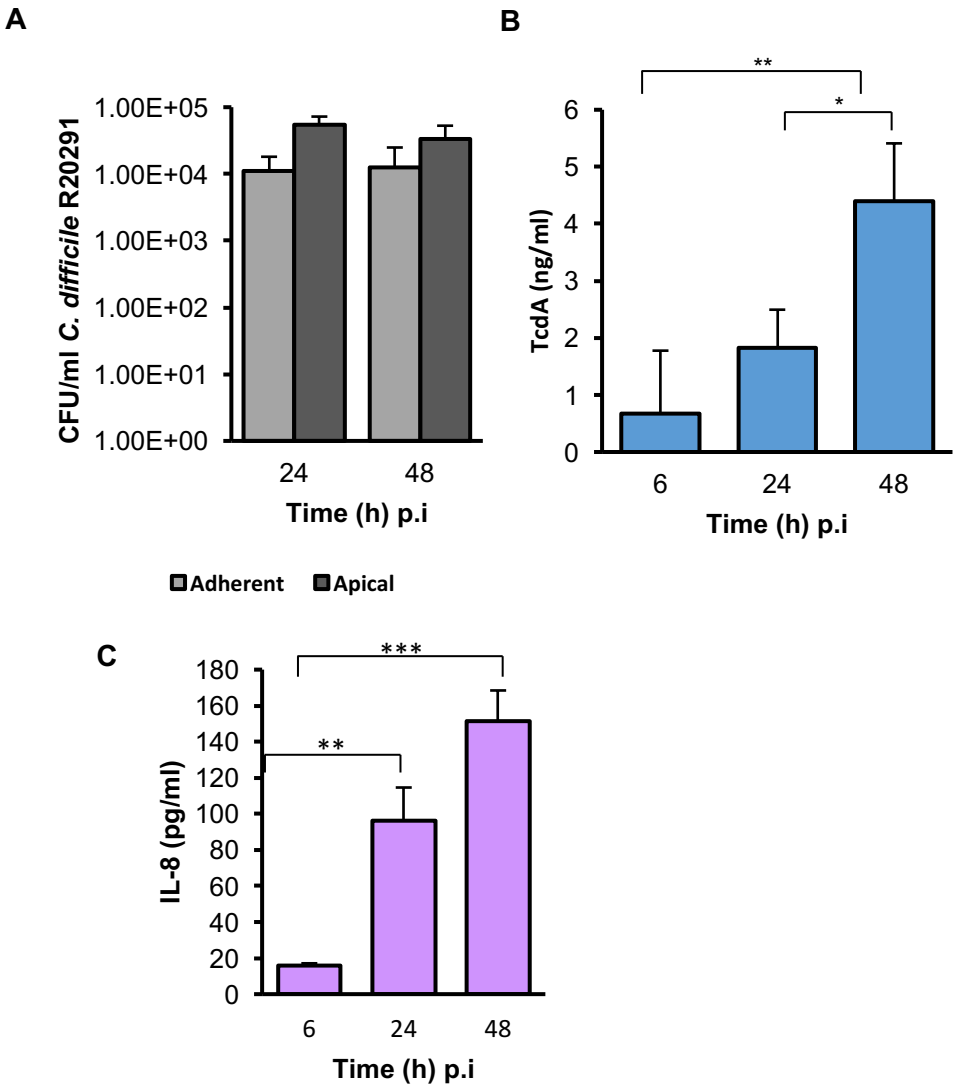

FIG 3. Production of *C. difficile* spores, toxins and host responses to infection. (A) Colony counts of spores recovered after heat treatment of the adherent *C. difficile* fraction and the apical supernatants in the 2-D epithelial model (B) ELISA for *C. difficile* toxin A shows increased toxin after extended infection (C). ELISA for human IL-8 indicates increased IL-8 production at 24h and 48h p.i.

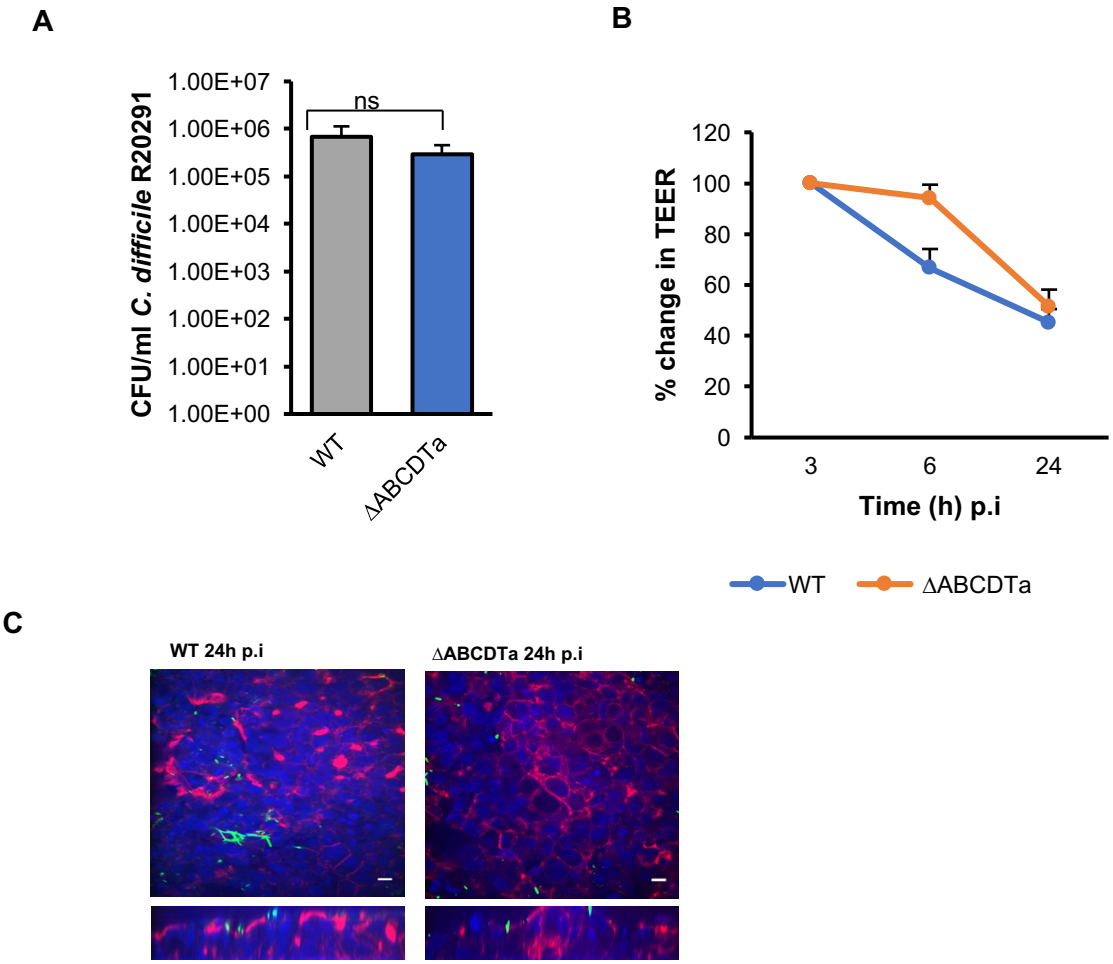

FIG 4. *C. difficile* toxins are not required for adherence to gut epithelial cells (A) Colony counts from epithelial cells infected with the WT R20291 and triple toxin mutant ($A^-B^-CDTa^-$) demonstrates that absence of the toxins does not affect adherence to the IECs (ns, not significant) (B) TEER values showing reduction at 24h p.i. between the WT and the triple toxin mutant. (C) Representative confocal microscopy images of IECs infected with the triple toxin mutant at 24h p.i. showing less redistribution of actin, stained with phalloidin (red) as compared to the WT. Inset shows the orthogonal XZ axis view of the IECs. *C. difficile* is stained green, actin, red and cell nuclei, blue, Scale bar = 10 μM.

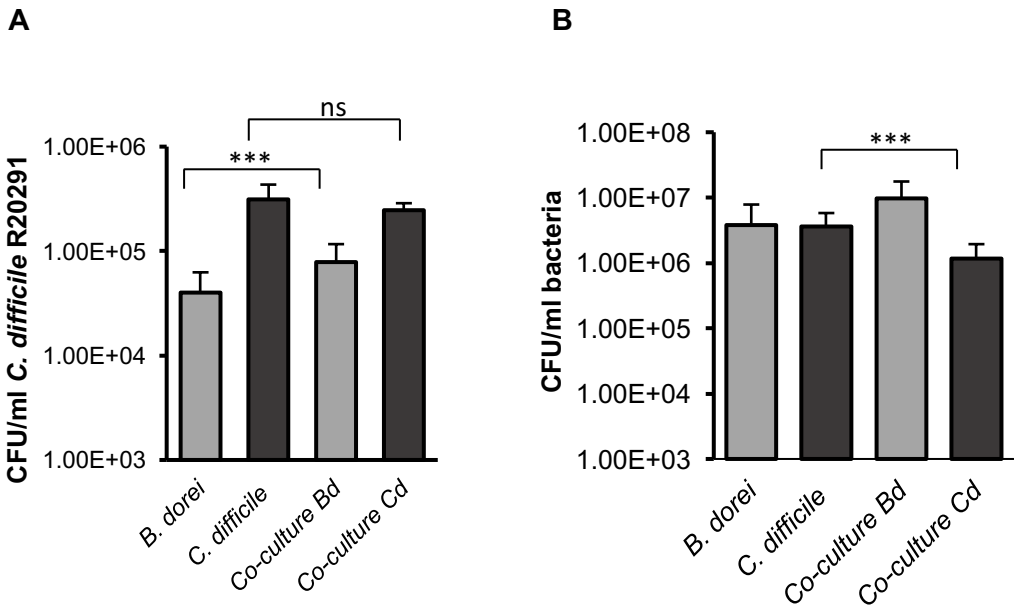

FIG. 5. Studying *C. difficile*-commensal interactions within epithelial models. (A) Co–culture studies of *B. dorei* with *C. difficile* in the VDC showed no significant inhibition at 3h p.i. (B) However, at 24h, a significant inhibition of *C. difficile* is observed. Co-culture Bd and Cd represents the growth of *B. dorei* and *C. difficile* respectively in the mixed culture (Bd, *B. dorei* and Cd, *C. difficile*). ***$p < 0.001$.

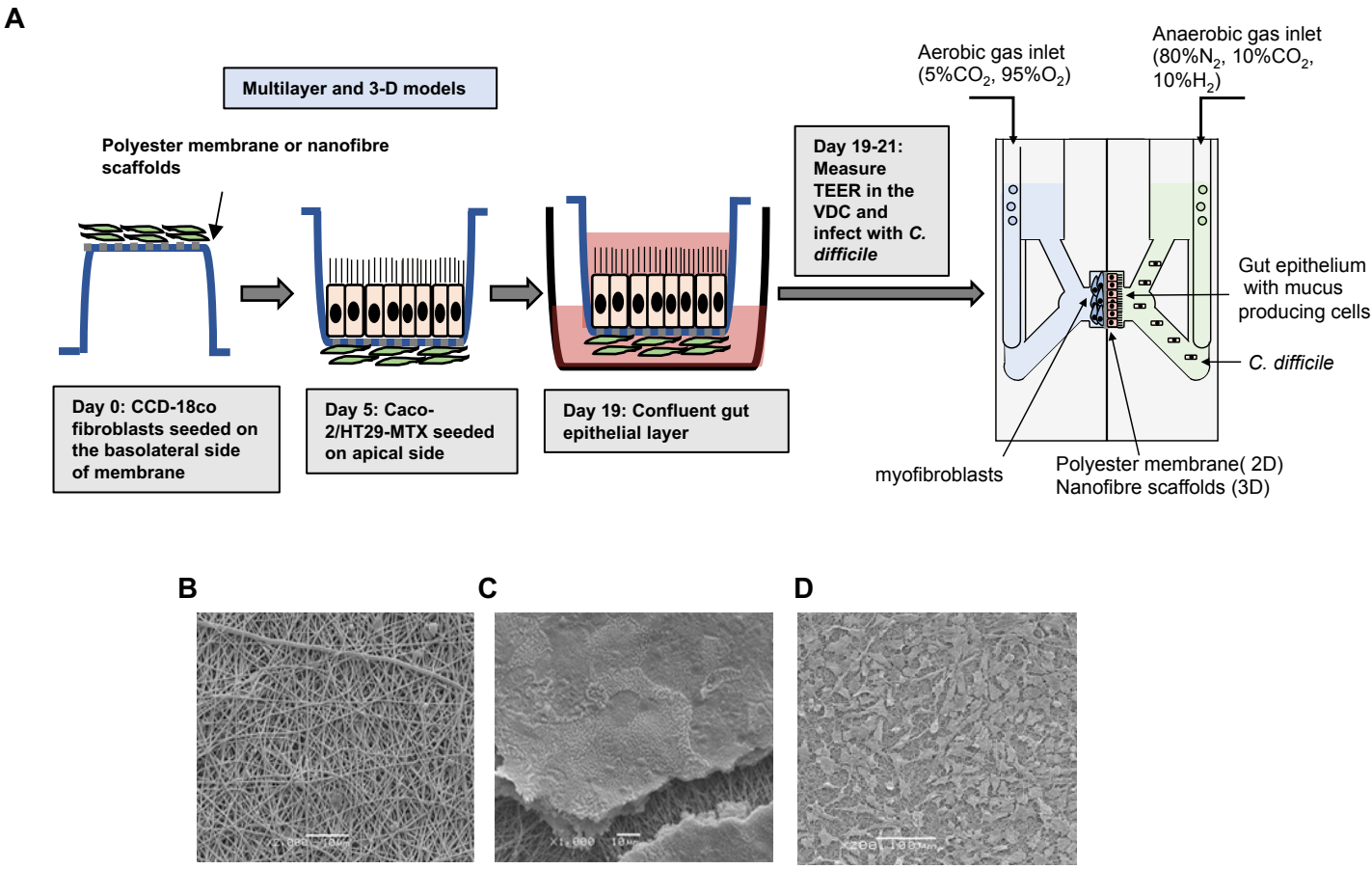

FIG 6. Scheme for generation of multilayer and 3-D models containing fibroblast cells and cell growth on the electrospun nanofibrous matrix (A) Fibroblast cells were first seeded on the basolateral side of the Snapwell or nanofiber scaffold for the multilayer and 3-D models for 5 days. Thereafter, IECs were cultured on the apical side for 2 weeks before placing the Snapwell filter between two halves of the chamber. *C. difficile* was infected apically while maintaining anaerobic conditions and the basolateral compartment was perfused with 5% CO_2 and 95% air. (B) Polyethylene terephthalate (PET; 10% *w/v*) was electrospun and exhibited a uniform nanofibrous matrix as determined by scanning electron microscopy. (C) Caco-2 epithelial cells were able to form a confluent monolayer on the nanofibrous scaffolds (the scaffold can be seen underneath the cells following processing for SEM). (D) The CCD-18co cells proliferated across the nanofibrous scaffold forming cell processes to adhere to the nanofibers.

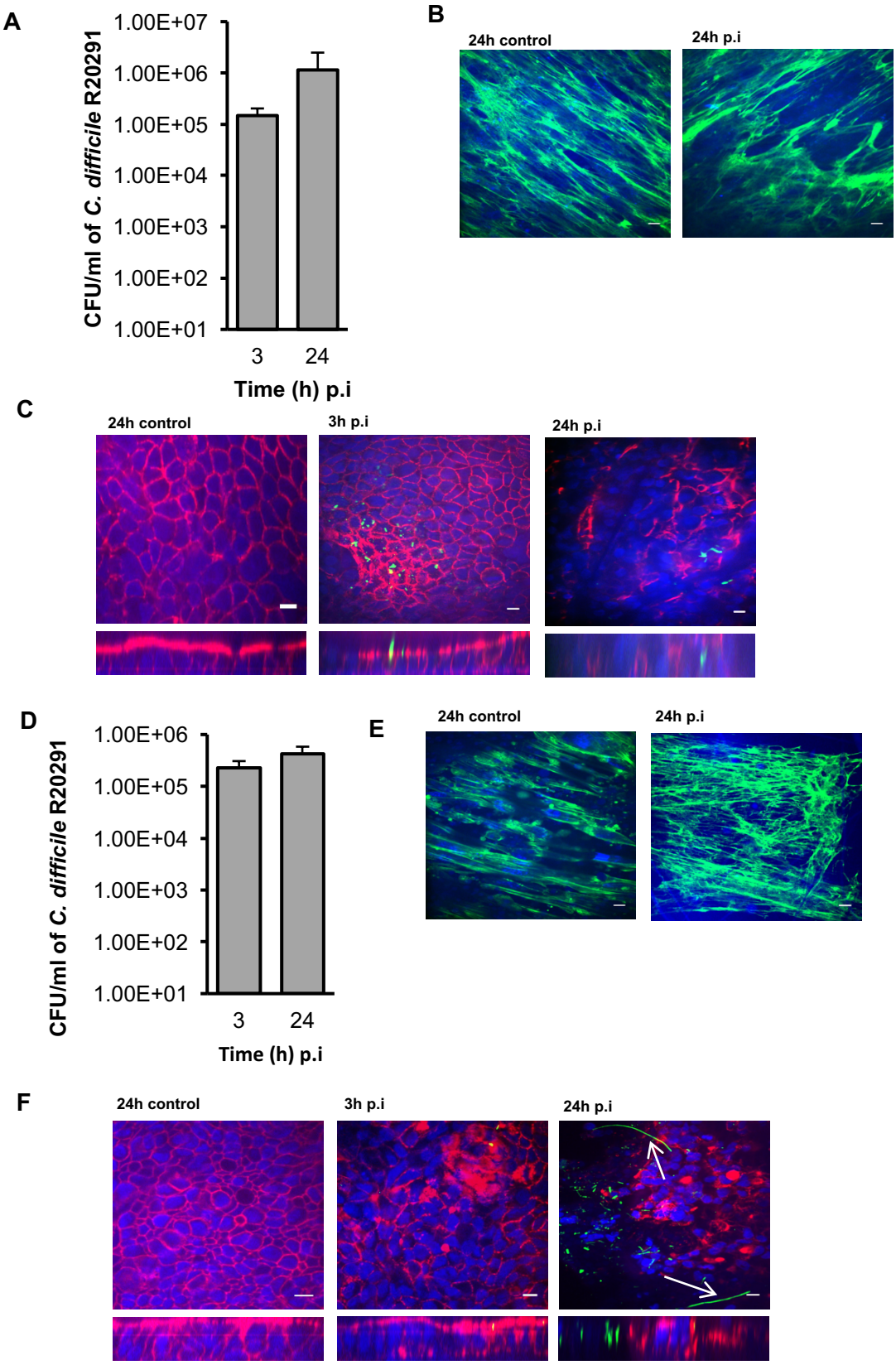
A
1.00E+07
1.00E+06
1.00E+05
1.00E+04
1.00E+03
1.00E+02
1.00E+01
CFU/ml of C. difficile R20291
3
24
Time (h) p.i
B
24h control
24h p.i
C
24h control
3h p.i
24h p.i
D
1.00E+06
1.00E+05
1.00E+04
1.00E+03
1.00E+02
1.00E+01
CFU/ml of C. difficile R20291
3
24
Time (h) p.i
E
24h control
24h p.i
F
24h control
3h p.i
24h p.i

FIG 7. Infection of *C. difficile* in multilayer and 3-D model leads to increased adhesion. Increased adherence of *C. difficile* in the multilayer and 3-D models, where fibroblasts are grown as a basolateral layer on polyester and nanofibers respectively. (A) Serial dilutions of the infected epithelial cell lysates were plated to determine the number of cell-associated bacteria in the multilayer model. (B) Anti-fibronectin (green) staining of fibroblast cells in the basolateral layer of the control and infected cells at 24h p.i showing degradation of the fibroblast layer in the multilayer model. (C) Representative images of *C. difficile* on the apical layer at 3h and 24h p.i. Inset shows the orthogonal XZ axis view of the IECs. *C. difficile* is stained green, actin, red and cell nuclei, blue, Scale bar = 10 μM. (D) *C. difficile* colony counts from infected cells in the 3-D model (E) Anti-fibronectin (green) staining of fibroblast cells in the basolateral layer at 24h p.i. (F) Immunofluorescent microscopy images of *C. difficile* infected IECs at 3h and 24h p.i in the 3-D model. *C. difficile* filamentous forms are observed at 24h p.i. (indicated by arrows). Inset shows the orthogonal XZ axis view of the IECs. *C. difficile* is stained green, actin, red and cell nuclei, blue, Scale bar = 10 μM.

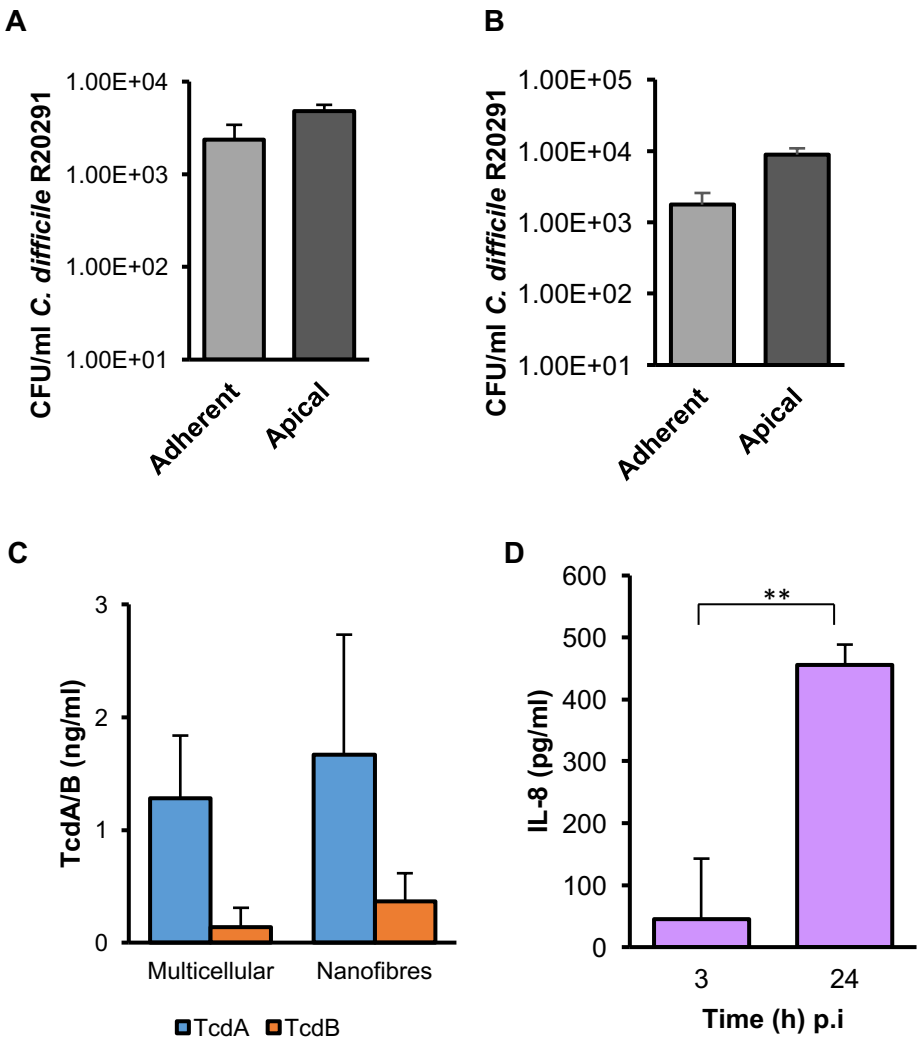

FIG 8. *C. difficile* spores and toxin production, and host response to infection in the multilayer and 3-D models. Colony counts of spores in the cell-associated *C. difficile* fraction and the apical supernatants in the (A) multilayer and (B) 3-D model. (C) Toxin A and B levels in the multilayer and 3-D model. (D) IL-8 levels are significantly increased in the 3-D model at 24h p.i., $^{**}p < 0.01$ as determined by the student t test.